April 13, 2010
Volume 43
Number 7

Macromolecules

pubs.acs.org/Macromolecules

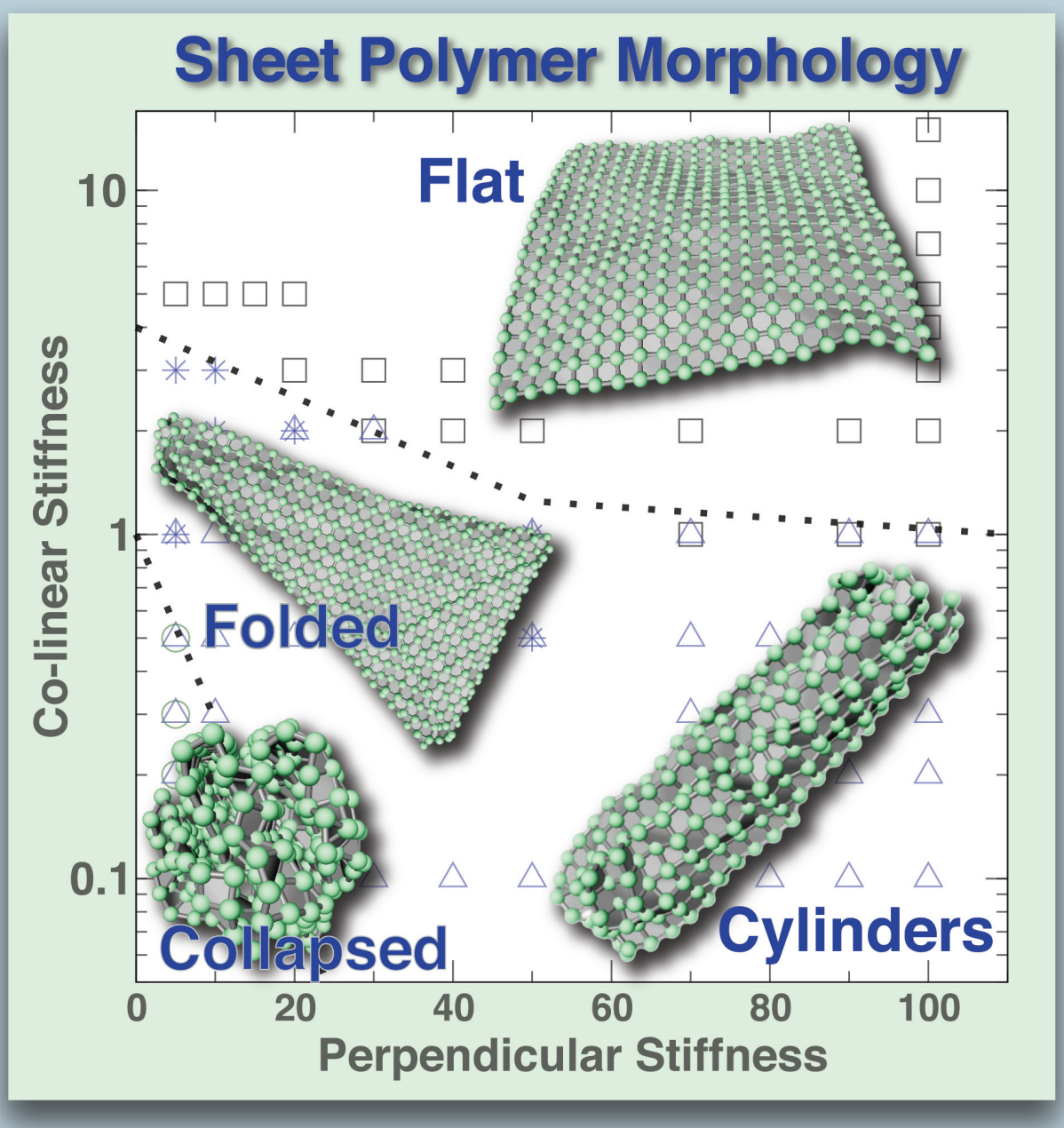

ACS Publications
High quality. High impact.
www.acs.org

3438 *Macromolecules* **2010**, *43*, 3438–3445
DOI: 10.1021/ma902081m

Macromolecules
ARTICLE

Morphology and Transport Properties of Two-Dimensional Sheet Polymers

Scott T. Knauert,[†] Jack F. Douglas,*[,‡] and Francis W. Starr*[,†]

[†]*Department of Physics, Wesleyan University, Middletown, Connecticut 06459, and* [‡]*Polymers Division, National Institute of Standards and Technology, Gaithersburg, Maryland 20899*

Received September 18, 2009; Revised Manuscript Received February 19, 2010

ABSTRACT: Whereas there has been extensive theoretical and experimental investigation of the properties of linear polymer chains in solution, there has been far less work on sheet-like polymers having 2D connectivity and 3D crumpled or collapsed shapes caused by thermal fluctuations, attractive self-interactions, or both. Sheet-like polymers arise in a variety of contexts ranging from self-assembled biological membranes (e.g., the spectrin network of red blood cells, microtubules, etc.) to nanocomposite additives to polymers (carbon nanotubes, graphene, and clay sheets) and polymerized monolayers. We investigate the equilibrium properties of this broad class of polymers using a simple model of a sheet polymer with a locally square symmetry of the connecting beads. We quantify the sheet morphology and the dilute-limit hydrodynamic solution properties as a function of molecular mass and sheet stiffness. First, we reproduce the qualitative findings of previous work indicating that variable sheet stiffness results in a wide variety of morphologies, including flat, crumpled or collapsed spherical, cylindrical or tubular, and folded sheets that serve to characterize our particular 2D polymer model. Transport properties are of significant interest in characterizing polymeric materials, and we provide the first numerical computations of these properties for sheet polymers. Specifically, we calculate the intrinsic viscosity and hydrodynamic radius of these sheet morphologies using a novel path-integration technique and find good agreement of our numerical results with previous theoretical scaling predictions.

Introduction

The study of the solution properties of linear polymer chains has formed the foundation of polymer science, and the characterization of polymer properties through a range of solution measurements remains a central activity in this field. Despite extensive study, polymer science is by no means a closed field, and there are many basic problems that remain open, especially in relation to the transport properties of polymeric systems.

In the present work, we focus on the less well-studied case of 2D, or "sheet" polymers, that is, polymers that have 2D connectivity but which can take a thermally crumpled or collapsed configurations in 3D space, similar to linear polymers. Thin elastic sheets form the basis for many materials across a wide variety of fields and length scales.[1−4] Such molecularly thin membranes can be "fluid" with dynamic connectivity or "tethered" with fixed connectivity.[5] Examples of 2D polymers include exfoliated and synthetic clay materials,[6−9] graphene[10] or graphite oxide sheets,[11−13] carbon nanotubes,[14−16] polymerized layers,[17] and a host of self-assembled biological membrane structures.

There has been extensive computational investigation of basic morphological and thermodynamic properties of tethered membranes or 2D sheet polymers starting from the seminal work of Kardar, Kantor, and Nelson,[18−20] the large scale computations of Abraham and Grest,[21−23] and later work by other authors.[24−30] Additionally, there are some analytic predictions for the behavior of hydrodynamic transport properties,[31] but these predictions have never been tested. Recent simulations have examined the dynamics of the crossover from subdiffusive to diffusive behavior of sheet polymers,[32−35] and some limited experimental studies have been performed to evaluate the intrinsic viscosity [η] of monolayer films of polymethylmethacrylate polymerized on substrates,[36,37] but surprisingly limited effort has been made to explore seriously the properties of this novel and promising class of polymer materials from both experimental and computational standpoints.

Here we investigate some of the basic solution properties required to characterize these materials, with an emphasis on transport properties that have not previously been computationally investigated. We restrict the polymer connectivity to the case of a square sheet, where the monomers within this manifold are connected by stiff springs that regulate the stiffness of these polymers. Many previous computations emphasized sheets having a local hexagonal symmetry, but 2D polymers with both hexagonal and square local symmetries arise physically,[38] and the sensitivity of the sheet properties to this internal connectivity constraint is a matter of interest. A hard core repulsion between the polymer beads, along with an attractive short-range interaction, is also incorporated into our sheet model. We examine the structures formed by these model sheet polymers via molecular dynamics simulation for a range of molecular mass, M.

As in the case of linear polymers, we see a range of extended and compact structures. Depending on the stiffness of the bonding parameters. The sheets exhibit flat, collapsed surface, compact closed, cylindrical, or folded sheet configurations in qualitative accord with prior work. As in the case of linear polymers, we quantify the equilibrium geometries of these structures by the scaling of the radius of gyration, R_g, with M.

Having established the morphologies of this model for sheet polymers, we characterize the transport properties by calculating the hydrodynamic radius, R_h, and intrinsic viscosity, [η], basic properties characterizing traditional polymers. We compute R_h

*To whom correspondence should be addressed. E-mail: jack.douglas@nist.gov; fstarr@wesleyan.edu.

 Published on Web 03/05/2010 © 2010 American Chemical Society

and [η] using an efficient path-integral method that makes these computations numerically feasible. We find that the numerical scaling relationships for these transport properties are consistent with scaling relations derived in ref 31, providing a consistent description of solution morphology and transport for low concentration solutions that generalizes the known relationships for linear polymers.

Ideally, this effort will stimulate effort to synthesize sheet polymers at well-defined mass, boundary shape, and topology so that these ideas can be directly experimentally tested. Experimental synthesis might proceed by adsorbing polymerizable material on surfaces,[36,37] perhaps patterned by alkane thiols to control sheet dimensions, followed by ultraviolet polymerization. Significant work remains to performed to determine how membrane shape, aspect ratio, interactions, and topology influences ratios of these properties, as in the familiar cases of ring, star, and comb topologies for linear polymers.[39]

Sheet Model and Simulation Details

Building on sheet models studied previously in the context of linear polymer/sheet composites,[40,41] we model sheet nanoparticles by a square grid of beads, with L beads along each edge, for a total of $N = L^2$ beads. Each bead interacts via a truncated and force-shifted Lennard-Jones (LJ) potential. We truncate the potential at a cutoff distance $r_c = 2.5\,\sigma$, where σ is the distance parameter of the LJ potential (roughly corresponding to bead diameter). This truncation includes a short-ranged attraction between beads of the sheet. Many earlier studies examined only repulsive excluded volume interactions; a modest attraction between units of the surface is expected for most experimentally realizable membranes and will play an important role in the formation of collapsed and folded structures. Additionally, many earlier works focused on six-coordinated hexagonal sheets. We find below that our four-coordinated square sheets exhibit the same qualitative morphologies and the same scaling exponents, so we expect the specific coordination to play only a secondary role.

Because we do not aim to study any specific system, we use reduced units where $\sigma = \varepsilon = m = 1$. ($\varepsilon$ is the LJ interaction strength and m is the bead mass.) Length is defined in dimensionless units relative to σ, time is in units of $\sigma(m/\varepsilon)^{1/2}$, and temperature T is expressed in units of ε/k_B, where k_B is the Boltzmann constant, and in reduced units, $k_B = 1$.

Beads are bonded to their nearest neighbors by a finitely extensible, nonlinear elastic (FENE) spring potential[42]

$$V_{\mathrm{FENE}}(r_{ij}) = -\frac{k_F R_0^2}{2}\ln\left(1-\left(\frac{r_{ij}}{R_0}\right)^2\right) \quad (1)$$

where we choose $k_F = 100$ and $R_0 = 1.5$, resulting in an equilibrium bond length 0.90.

In this work, the sheet stiffness is described by two additional potentials

$$V_{\mathrm{lin}}(\theta_1) = K_{\mathrm{lin}}(1+\cos\theta_1) \quad (2)$$

and

$$V_{\perp}(\theta_2) = \frac{K_{\perp}}{2}\left(\theta_2 - \frac{\pi}{2}\right)^2 \quad (3)$$

where θ_1 is the angle among the three roughly colinear consecutive beads on the sheet, and θ_2 is the angle among three roughly perpendicular connected beads, as illustrated in Figure 1. We vary K_{lin} and $K_{\perp}$ to explore basic configurational classes of these 2D polymers.

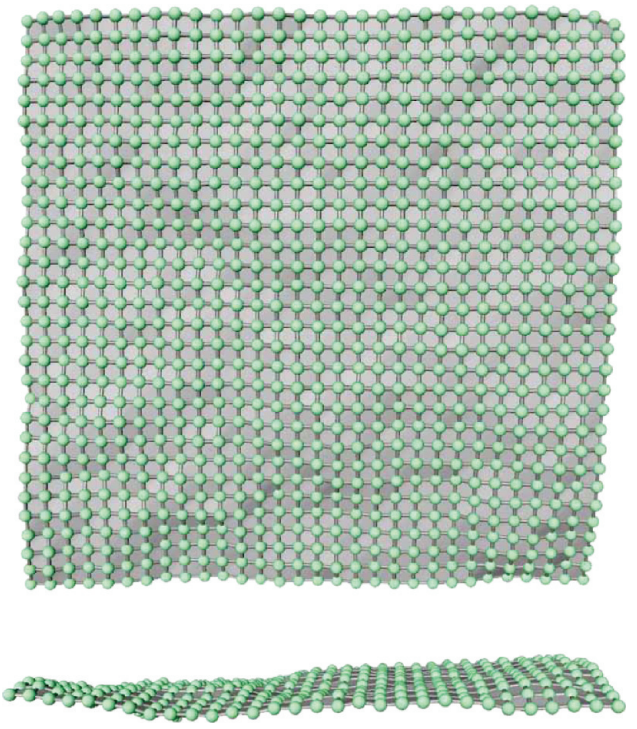

Figure 1. Front and profile views of a sheet with a roughly "flat" morphology. Specifically, this is the case $L = 30$ ($N = 900$), $K_{\mathrm{lin}} = 15.0$ and $K_{\perp} = 100$. The sheet beads are rendered as spheres connected by cylinders, representing FENE bonds.

We investigate the morphology of tethered sheets by equilibrium molecular dynamics simulations for ensembles of different initial conditions. For all cases, we use periodic boundary conditions and choose the system size to be twice the edge length, L, so that no force site on the sheet will interact with the periodic image of any other force site on the sheet, thereby approaching the dilute limit. To control temperature, T, we use the Nosé−Hoover thermostat. We select the "mass" of the thermostat $Q = 6NT/\omega^2$, where $\omega = 234.09$ is the intrinsic frequency obtained from a theoretical calculation for a face-centered cubic LJ system,[43] a natural frequency for the heat bath. All data presented are for simulations at $T = 1.0$. Varying T should not qualitatively effect the morphologies we find but will effect the value of the sheet stiffness at which the sheets collapse into more compact structures. We integrate the equations of motion via the reversible reference system propagator algorithm (rRESPA), a multiple time step algorithm used to improve simulation speed.[44] A basic time step of 0.002 is employed for a three-cycle version of rRESPA with forces divided into "fast" intramolecular bonded forces (V_{FENE}, V_{lin}, $V_{\perp}$) and "slow" intermolecular nonbonded components.

Sheet Morphology Types

By varying the linear stiffness, K_{lin}, and perpendicular stiffness, $K_{\perp}$, we explore basic equilibrium morphologies of the sheets. It is necessary to establish the possible morphologies for our model so that we may later connect these with the transport properties. To quantify the sheet morphology, we investigate how the mean-squared radius of gyration[45]

$$R_g^2 \equiv \frac{1}{2M^2}\left\langle \sum_{i,j=1}^{N} (\vec{r}_i - \vec{r}_j)^2 \right\rangle \quad (4)$$

depends both on sheets stiffness and molecular mass. The angular brackets denote an average of many independent configurations.

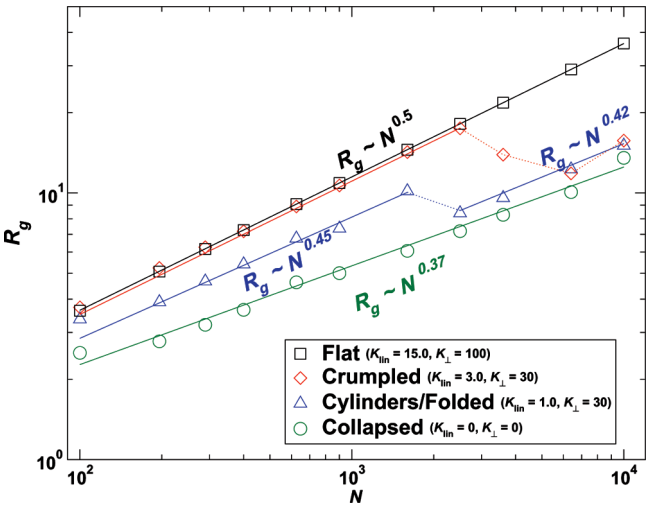

Figure 2. R_g scaling of the dominant observed morphologies. Note that for $N \gtrsim 1600$ ($L \gtrsim 40$), the crumpled and folded sheets undergo a change in morphology. See the text for further discussion.

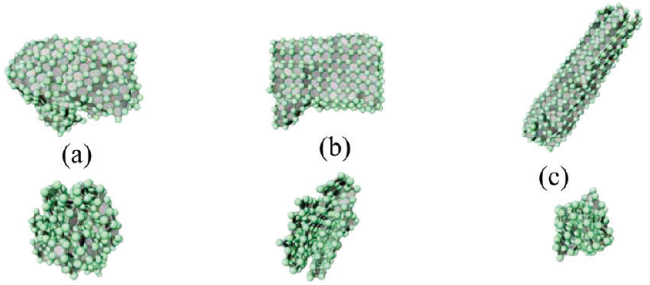

Figure 3. Front and profile views of the three $L = 20$ collapsed morphologies: (a) the "ball" with the smallest observed R_g values; (b) the "stacked" configuration, so named because it resembles a neatly folded sheet pressed flat into a stack; (c) the cylinder, which has the largest R_g values.

In our case, because all beads have the same mass, $m = 1$, the total sheet polymer mass, M, may be replaced by the total number of beads, N.

The scaling of R_g with N defines fractal dimension, d_f . Following polymer physics convention, we define the scaling relation[46]

$$R_g \approx N^{\nu} \tag{5}$$

where $\nu = 1/d_f$.

By varying K_{lin} and $K_\perp$, we can generate a number of different morphologies with our sheet model. Here we limit our discussion to four main cases: (i) "collapsed" sheets that are nearly space filling with $K_{lin} = 0$, $K_\perp = 0$; (ii) flat sheets with $K_{lin} = 15.0$, $K_\perp = 100$; (iii) "crumpled" sheets (nearly flat) with $K_{lin} = 3.0$, $K_\perp = 30$; and (iv) "folded" sheets with $K_{lin} = 1.0$, $K_\perp = 30$. To characterize the sheet shape from the scaling relation in eq 5, we investigate edge lengths $L = 10$, 14, 17, 20, 25, 30, 40, 50, 60, 80, and 100. A summary of the dominant behaviors for R_g and ν is illustrated in Figure 2. We expand on these results below.

Collapsed Sheets. Setting both K_{lin} and $K_\perp$ at or close to 0 results in highly flexible sheets. In this case, the Lennard-Jones attractions cause the sheets to crumple to a nearly fully collapsed state. These collapsed sheets form either roughly spherical or cylindrical objects depending on the initial conditions, and Figure 3 illustrates some representative configurations.

To determine the frequency of these states, we perform 50 runs at each L and calculate the distribution $P(R_g)$ of R_g values. Figure 4 shows that there is significant gap between the roughly spherical objects and the cylinders for $N = 400$. We take advantage of this gap to study separately the morphological properties of the spherical and cylindrical objects, which we extend to a broader range of sheet stiffness values. Specifically, we performed ten further runs each at parameter values ($K_{lin} = 0.1$ and $K_\perp = 5$), ($K_{lin} = 0.1$ and $K_\perp = 10$), and ($K_{lin} = 0.5$ and $K_\perp = 5$) over the size range $100 \leq N \leq 2500$. Evidently, all of these systems exhibit a propensity to form either compact spherical or cylindrical objects, which we analyze separately below to obtain the eight different data sets shown in Figure 5. The spherical objects have $\nu = 0.37 \pm 0.03$, and thus $d_f = 1/\nu = 2.7 \pm 0.2$.[47] Although these structures are relatively collapsed, they are not truly space-filling objects, at least at the edge lengths studied. The cylindrical objects have $\nu = 0.45 \pm 0.02$, and a correspondingly lower fractal dimension, $d_f = 2.22 \pm 0.05$.

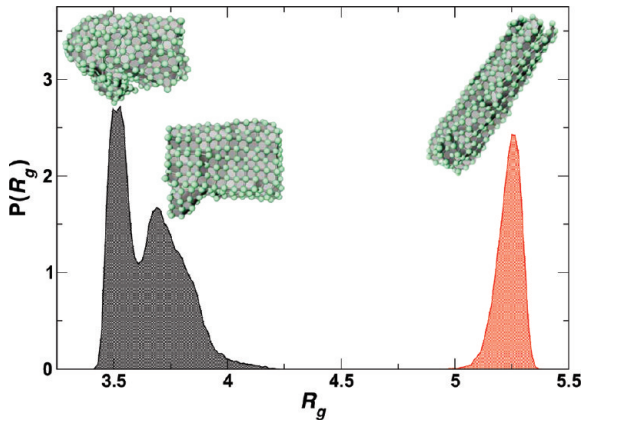

Figure 4. Frequency of various collapsed morphologies. The R_g values for $L = 20$ sheets with $K_{lin} = 0$ and $K_\perp = 0$ are divided into two separate regions. The small R_g sheets are roughly spherical, and the large R_g sheets are cylindrical. The distribution is more complex where the small R_g distribution is bimodal. Further investigation shows the presence of both "ball" and "stacked" sheet types.

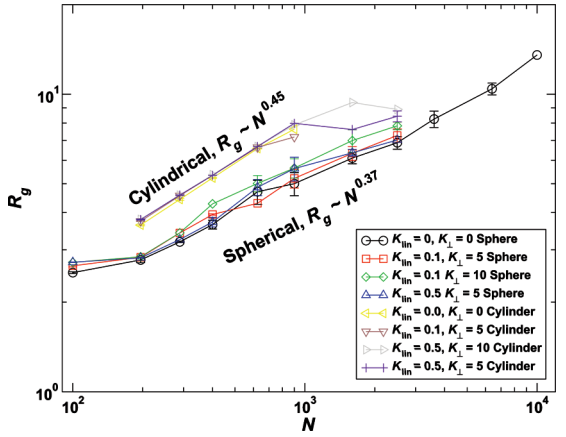

Figure 5. Scaling of R_g for the various collapsed sheet systems investigated. Each set of runs produced distributions that were bimodal at small N but become unimodal at large N. This corresponds to a N value at which R_g of the initially cylindrical objects collapses.

Flat and Crumpled Sheets. Using large values of K_{lin} and $K_\perp$ leads to stiff extended sheets that are only slightly crumpled. Figure 1 illustrates a typical configuration for an $L = 30$ sheet with $K_{lin} = 15.0$ and $K_\perp = 100$. Unlike the collapsed sheets, the initial conditions do not have an effect on the average value of R_g. In other words, $P(R_g)$ (not shown) is unimodal about a single flat morphology. The

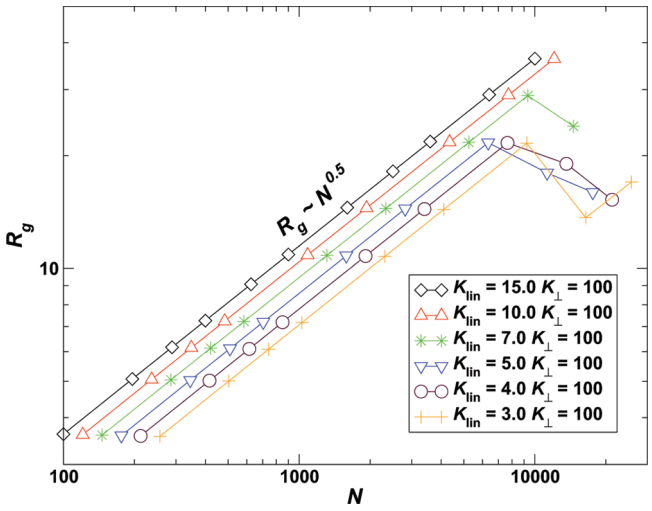

Figure 6. Scaling of R_g for the various flat sheet systems investigated. The scaling relation for perfectly flat sheets is plotted for comparison. For all flat sheets, $R_g \approx N^{0.5}$ associated with flat objects. Because our simulations produce nearly identical values of R_g, we progressively shift each data set by a factor 1.2 for the clarity of the Figure.

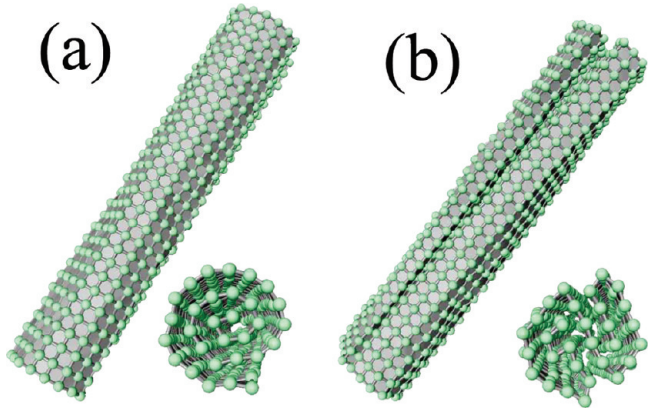

Figure 7. Front and profile views of (a) a single spiral cylinder and (b) a double spiral cylinder. For both cases, $L = 30$ cylindrical sheet, $K_{lin} = 0.1$, and $K_\perp = 90$.

lack of dependence on initial conditions is explained by the fact that the larger stiffness parameters in the flat sheets oppose any deviations from a flat morphology, preventing any folds from occurring.

Figure 6 shows the scaling behavior of R_g for a variety of parameter values, all of which yield flat sheets; that is, $\nu = 0.500 \pm 0.005$ or $d_f = 2.00 \pm 0.02$. For $N > 3600$, the scaling relation breaks down for sheets with smaller K_{lin}. Decreasing $K_\perp$ has a similar effect. This breakdown is the result of a sheet collapsing and is a general feature of our model for sufficiently large N. Because the stiffness parameters are defined locally, K_{lin} and $K_\perp$ effectively define a persistence length for the sheets. If L is large enough, an arc may form, and if the end points of the arc are within the range of attraction of each other, the edges can "stick" to each other, giving rise to a fold in the sheet. Therefore, any sheet will collapse for large enough L. Moreover, as K_{lin} increases, the N value at which the scaling relation in eq 5 breaks down becomes larger.

Transitional Morphologies: Tubules and Folded Sheets. A large number of parameter choices yield primarily cylindrical objects. Figure 7 shows single and double spiraled tubules, the dominant transitional morphologies between the collapsed and flat morphologies. These structures are often referred to as tubules in the literature.[48−50] Figure 8 shows the scaling of

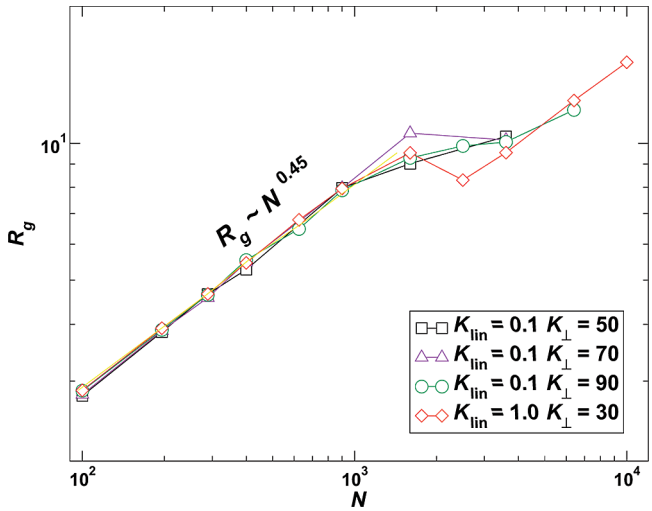

Figure 8. Scaling of R_g for cylindrical morphologies for values of K_{lin} and $K_\perp$ between those of the collapsed and flat morphologies. There is one exception: the $K_{lin} = 1.0$, $K_\perp = 30$ system produces a visually "folded" morphology, but the scaling behavior is indistinguishable.

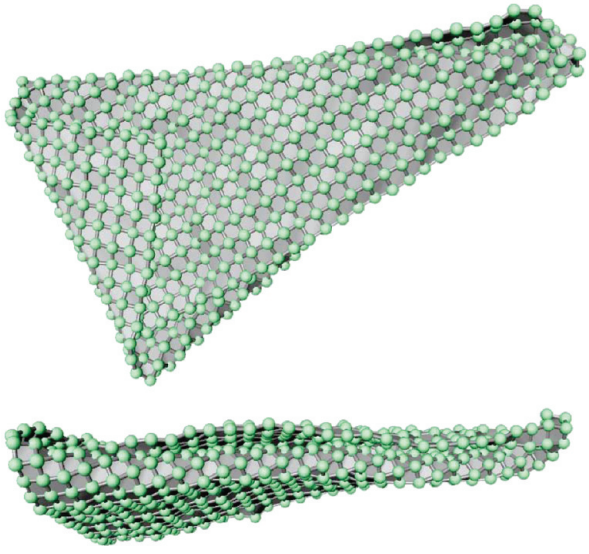

Figure 9. Front and profile views of a "folded" sheet with $L = 30$, $K_{lin} = 1.0$, and $K_\perp = 30$.

R_g for several choices of K_{lin} and $K_\perp$. Individual samples exhibit either one or two spirals. As in the case of cylinders formed for parameter values that yield collapsed structures, these cylinders have $\nu = 0.45 \pm 0.02$. Such transitional objects have previously been found to have similar ν values in the range between 0.4 and 0.42[25,26] for simulations of hexagonal sheet polymers at a compensation point (or theta point) between repulsive and attractive interactions (which favor flat or collapsed states, respectively). Similar to the flat sheets, for large enough N, we find that the transitional states are no longer stable, and the sheets collapse. However, we lack sufficient data to evaluate the large-N scaling behavior for these structures, which we expect will be similar to that of the previously described collapsed structures. An additional morphology emerges in this parameter range: wedge-shaped structures similar to what the literature refers to as a "folded" sheet.[51] Figure 9 shows that this folded morphology is dominant at ($K_{lin} = 1.0$ and $K_\perp = 30$) and ($K_{lin} = 3.0$ and $K_\perp = 10$). Whereas this morphology appears to be visually distinct, the scaling behavior is the same as that for the cylinders.

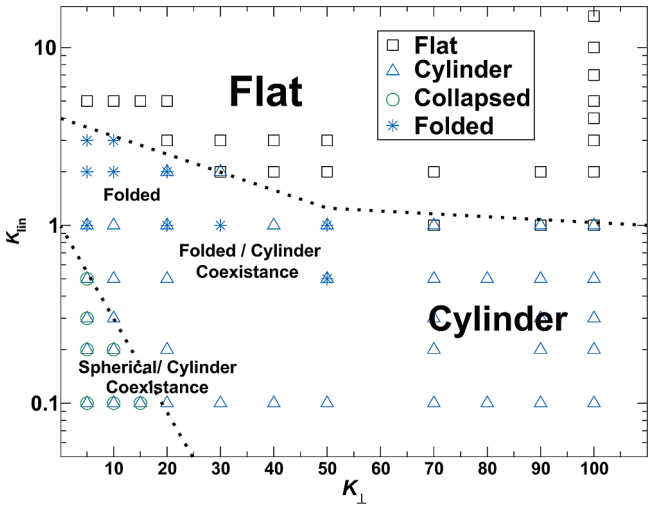

Figure 10. Approximate "sheet morphology phase diagram" is shown for $N = 400$ ($L = 20$) as a function of K_{lin} and $K_\perp$.

Morphological Phase Diagram. We perform an exhaustive set of simulations to summarize how K_{lin} and $K_\perp$ affect the morphology and use that information to create a "sheet phase diagram" (Figure 10) for one edge length (for $L = 20$, $N = 400$). The sheet morphologies can be classified into three main regions: (i) a collapsed region at small stiffness where both spherical and cylindrical morphologies coexist, (ii) a flat region at high stiffness, and (iii) a transitional region where cylinders are the dominant morphology but wedge-shaped of other folded morphologies are also present.

Whereas there is a stable transition region between flat and collapsed states for $L = 20$, we know from our previous examination of the exponent scaling (for a more limited set of stiffness parameters) that the larger sheets tend to collapse. This raises the question of whether the crossover from flat to collapsed sheets is always a continuous one, or if it might become discontinuous under some circumstances. Previous works[25,26] suggest that the transition is likely to be discontinuous when the sheets are highly flexible but that it is continuous for stiffer sheets, where coherent folds can form more easily. Indeed, Figure 10 shows that the region of folded structures shrinks as we decrease the sheet stiffness. However, a complete analysis of the phase space also requires a consideration of the N dependence of these morphologies. On the basis of the more limited simulations we have for larger N, we do not see qualitative changes in structure of the morphology diagram, and the crossovers between different regions vary in a similar way as the case of linear polymers upon varying polymer mass. Specifically, the regions of collapsed and cylindrical configurations expand as edge length grows, which we expect because the larger sheets can more easily fold on themselves. However, the transition cylinder/folded region appears to somewhat shrink with increasing mass. This may be indicative of a potential discontinuity from collapsed to flat sheets for very large N but is by no means conclusive. The complete N dependence is a valuable question to examine in future work but promises to be computationally challenging.

Transport Properties

Having established the basic morphologies and their approximate mass scaling for our model, we next evaluate basic hydrodynamic properties of these sheet polymers important for their solution characterization, and connect it back to sheet morphology. The highly extended nature of linear polymer chains in the swollen state makes polymer chains effective at modifying the viscosity of the solute to which they are added. The diffusion of such large objects in solution is slow in comparison with the monomers comprising the polymer. These changes in diffusivity are also evident for 2D polymers, although the effect of swelling can be expected to be larger for linear polymers because their conformations are more susceptible to thermal fluctuations.

Intrinsic Viscosity. The intrinsic viscosity $[\eta]$ defines the differential change of viscosity, η, when a polymer is added to solution in the dilute limit. The influence of polymer branching and stiffness on $[\eta]$ for linear polymers has been extensively investigated both theoretically and experimentally.[39] In this section, we consider an extension of this work to 2D polymers. Formally, the ratio of viscosity of a polymer solution, η, to the pure solvent, η_s, can be expanded in terms of a power series in the polymer concentration, ϕ

$$\eta/\eta_s = 1 + [\eta]\phi + \mathcal{O}(\phi^2) \tag{6}$$

We utilize a numerical path integral package (ZENO) that allows for simultaneous computation of $[\eta]$ based on geometric information about the particle shape.[52] ZENO calculates the transport properties of complex-shaped particles by exploiting an analogy between hydrodynamics and electrostatics.[53] Mathematically, this computational method is based on the observation that an angular preaveraging of the Green's function for the steady-state Naiver−Stokes equation (the Oseen tensor) is exactly the Green's function for the Laplace equation. There are many interrelations between electrostatic and hydrodynamic properties that derive from this analogy. The most notable is that for objects of fixed shaped having "stick" hydrodynamic boundary conditions, $[\eta]$ is proportional to the intrinsic conductivity, $[\sigma]$, and hydrodynamic radius, R_h, is proportional to capacity, C, for highly conducting objects having the same shape to a high degree of approximation.[52,53] The interrelations between these fundamental hydrodynamic and electrostatic "shape functionals" ultimately derive from a similar mathematical formulation of their boundary value problems. Because C and the electric polarizeability tensor can be calculated formally by averaging over random walk trajectories,[52−55] we can compute $[\sigma]$ and C of our sheet polymers directly from one calculation and then estimate $[\eta]$ and R_h (see next section) to a good approximation.

The calculation of $[\sigma]$, a byproduct of our calculation of $[\eta]$, has independent interest in the description of conductivity changes arising when conducting sheet particles (e.g., graphene) are added to a relatively insulating material (e.g., most polymeric materials). Additionally, because C is proportional to the Smoluchowski rate constant for diffusion-limited reactions,[56] C is predictive of the rate of heat transfer and reaction rates for diffusion-limited reactions. The mass scaling of $[\sigma]$ and C should follow that of $[\eta]$ and R_h, respectively. Apart from theoretical interest, these property interrelations offer additional methods for characterizing sheet polymers and insight into the optimal design of material using sheet polymer additives such as graphene.

Figure 11 shows $[\eta]$ as a function of the sheet size, N. The scaling behavior of $[\eta]$ can be understood on the basis of a generalization of Kirkwood−Riseman theory[39] to sheetlike morphologies. Specifically, $[\eta]$ should scale as[31]

$$[\eta] \approx N^{(d-2)\nu-1} R_g^2 \tag{7}$$

where d is the spatial dimension. Combining with eq 5, we obtain the expected asymptotic scaling

$$[\eta] \approx N^{3\nu-1} \tag{8}$$

for $d = 3$, just as in the case of flexible polymers.

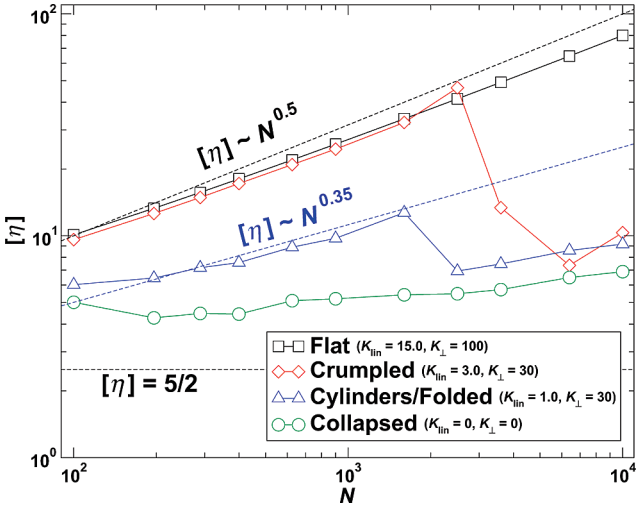

Figure 11. Intrinsic viscosity, $[\eta]$, as a function of sheet size. The dotted lines indicate theoretically predicted scaling behaviors. Note that the collapsed sheets have nearly constant $[\eta]$; for comparison, $[\eta] = 5/2$ is the theoretical Einstein value for a hard sphere.

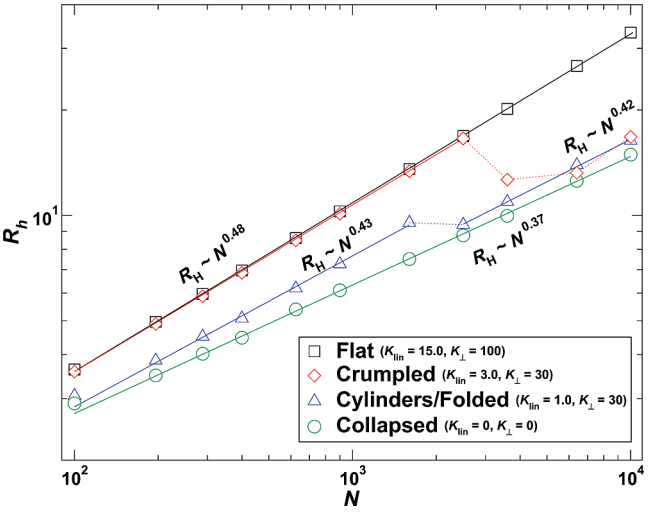

Figure 12. Hydrodynamic radius, R_h, as a function of sheet size. The scaling with N directly tracks the variation of parallels that of R_g in Figure 2.

Because we know ν from the previous section, we can test the validity of this scaling relation. The flat and crumpled sheets have $\nu = 0.500 \pm 0.005$, and so we expect $[\eta] \approx N^{0.500\pm0.015}$, matching the theoretical predictions. When the crinkled sheets collapse ($N \gtrsim 3600$), $[\eta]$ approaches the value for the crumpled sheets. The collapsed sheets have $\nu = 0.37 \pm 0.03$, and so we expect $[\eta] \approx N^{0.11\pm0.09}$, that is, nearly independent of N; our results for $[\eta]$ for collapsed sheets are consistent with a nearly N-independent behavior. Moreover, because the collapsed sheets are roughly spherical, it follows naturally that $[\eta]$ should be close to that theoretically known value for the sphere, $[\eta] = 5/2$, independent of N.[57,58] The transitional cylindrical and folded sheets have $\nu = 0.45 \pm 0.02$, and so we expect the scaling $[\eta] \approx N^{0.35\pm0.03}$; our results are consistent with this scaling theory prediction prediction for $N \leq 1600$. At larger N, the sheets collapse, and the value of $[\eta]$ is again similar to that of the collapsed state.

Hydrodynamic Radius. The translational diffusion coefficient, D, of a 2D polymer or any Brownian object embedded in three dimensions is defined by the general Stokes–Einstein relationship

$$D = \frac{k_B T}{6\pi\eta R_h} \tag{9}$$

where $k_B T$ denotes thermal energy and R_h is the particle hydrodynamic radius. R_h also provides a measure of the effective particle "size" in solution. As in the case of $[\eta]$, the computation of R_h is a difficult problem for objects that are not spherical (or ellipsoidal), and there is indeed no accurate analytic method for computing R_h for flexible linear polymers even without excluded volume interactions. Fortunately, the ZENO package also allows for a numerical evaluation of R_h, regardless of the molecular complexity and topological form of the polymer.

We show the scaling behavior for R_h for the various sheet morphologies in Figure 12. Interestingly, the scaling of R_h roughly follows the scaling of R_g in Figure 2; the exponent value ν_h for the R_h scaling is consistently larger by 0.01, and the ratio R_h/R_g for the range of N studied is $0.9 \lesssim R_h/R_g \lesssim 1$. The scaling of R_h is more complicated for linear polymers, where a greater hydrodynamic permeability makes the apparent mass scaling exponent, ν_h, depend on M and monomer structure.[59] In particular, ν_h for good polymer solutions, where the flexible polymers chains are swollen by excluded volume interactions, is often found to be substantially smaller than ν obtained from measurements of R_g and other static property estimates of the chain dimensions. The ratio R_h/R_g is in the range reported for long polymer chains. Specifically, recent path integration computations indicate that $R_h/R_g \approx 0.7$ for self-avoiding linear chains, and $R_h/R_g \approx 0.85$ for ring self-avoiding polymers in the limit of infinite chain mass.[59] For spheres, this ratio is $(5/3)^{1/2} \approx 1.3$, so the sheets are intermediate between spheres and the more diffuse random coil polymers. Dendrimer molecules for modest generation numbers (three to five) and other branched macromolecules are predicted to have R_h/R_g ratios similar to those of our sheets.[60]

Conclusions

For a square-sheet polymer model, we have mapped out how the stiffness influences equilibrium morphology, as defined through the radius of gyration. More significantly, we provide basic solution transport properties and connect the scaling of $[\eta]$ to the sheet morphology. Our results confirm that we can reproduce the range of known morphologies: collapsed, flat, crumpled, cylindrical, and folded. These basic morphologies have been observed before[2,48−50,61] in simulations of 2D polymers having a hexagonal lattice connectivity, so these morphologies are apparently general. For a given edge length, L, varying the stiffness parameters K_{lin} and $K_\perp$ controls which morphology is dominant. At small K_{lin} and $K_\perp$, the sheets collapse, forming either spherical and cylindrical objects. As the stiffness $K_\perp$ increases, cylindrical objects become the dominant morphology (Figure 10). The behavior in this region is more complex, though, because folded objects are also present. For the flat morphologies, we have $\nu = 0.5$, the expected value for a flat plate. For flat sheets near the boundary between the flat and cylinder or folded morphologies, the sheets visually display some "crinkling", but ν does not deviate from the flat value. Because the bending parameters define an effective length scale for the sheet stiffness, the attractive interactions between beads will cause all sheets to collapse at large enough N. Had we used purely excluded volume interactions, this collapse would probably not occur on increasing sheet size. However, a modest self-attraction of the surface is plausible for most experimentally realizable membranes and facilitates the formation of complex folded structures.

The most novel aspect of the present work is the computation of the transport properties of membrane polymers. The intrinsic viscosity, $[\eta]$, shows a clear qualitative trend in stiffness: the stiffer and the more extended the sheet, the larger $[\eta]$ and R_h become. Moreover, the scaling of these transport properties directly follow theoretically expected scaling relations based on the Kirkwood−Riseman theory so that the slow crossover scaling that makes the static and dynamic scaling exponents different does not exist for sheet polymers.[59] Presumably, strong intra-sheet hydrodynamic interactions are responsible for this important effect.

Because we have focused on symmetric square sheets, it is natural to ponder to what degree anisotropy of the sheets might affect our results. For real membranes with modest anisotropy, we expect the scaling exponent values we find to be universal. This is supported by experiments on exfoliated graphite[11,12] where there is anisotropy. However, the prefactors and the exponent associated with the number of flexible sheet polymer configurations should be dependent on boundary shape, similar to the effect of varying topology (ring, star, comb) in linear polymers. For the case of sheets with extreme anisotropy, we can gain some insight by considering limiting situations. For example, when the sheet is only a single bead or few beads wide and repulsive self-interactions are predominant, the sheets must reduce to self-avoiding walks, which have an exponent ν near the Flory estimate of 3/5 in three dimensions. Therefore, a large anisotropy in the sheet coordinates progressively favors a stronger repulsive polymer self-interaction and ν values larger than the flat sheet value of 1/2. Additionally, sheet punctures, or technically "genus", may affect the exponent behavior.

Whereas we have focused on the dilute limit in this initial study, intersheet interactions can be significant and sometimes dominate the properties of real systems. We have carried out some preliminary calculations for multisheet systems and find that significant clustering of the sheets occurs, and this clustering can actually change the sheet morphology from that observed in the dilute limit. When clustering results in stacked layers, we anticipate a significant decrease in η and $[\eta]$. The formation of more open clusters (fractal, flat sheet, or rodlike) should have the effect of increasing η and $[\eta]$ because of the increase in the effective particle size. Therefore, changes in transport properties with aggregation should depend on the types of clusters formed. An investigation of the nature of entanglement in sheetlike systems would also be of interest, and simulations of sheets at high concentrations could provide some essential insight into this phenomenon.

Finally, we point out that tethered sheets generalizing linear chain block copolymers offer the possibility of diverse structures with singular properties and states of organization. For example, different types of copolymer materials could be obtained by controlling the outer shape of the sheet, the sheet topology, and by varying the chemical nature and shape of regions internal to the sheet manifold to create structures that self-associate into functional 3D folded structures whose form could be actuated thermodynamically. It should also be possible to make hybrid structures between the sheet and linear polymer chains by grafting a brush onto one side of the tethered sheet to create a "carpet" structure.

Given the enhanced barrier properties and encapsulation properties of sheet structures, these new types of polymers could have diverse applications and their study promises to be rich both experimentally and theoretically. Making this type of polymer should be facilitated by advances in self-assembled monolayer printing technology that should allow the facile formation of imprinted patterns onto which different monomer types can be adsorbed and subsequently polymerized.[17] Creating large quantities of monodisperse polymers of this type would be a challenge, but the potential applications of this new class of polymers and its potential scientific value should make this effort worthwhile.

Acknowledgment. We thank Wesleyan University for computer time, which was supported by National Science Foundation grant CNS-0619508. This work was supported by National Science Foundation grant DMR-0427239.

References and Notes

(1) *Statistical Mechanics of Membranes and Surfaces*; Nelson, D. R., Piran, T., Weinberg, S., Eds.; World Scientific: Singapore, 2004.
(2) Bowick, M. J.; Travesset, A. *Phys. Rep.* **2001**, *344*, 255.
(3) Wiese, K. J.; David, F. *Nucl. Phys. B* **1997**, *487*, 529.
(4) Gompper, G.; Kroll, D. M. *J. Phys.: Condens. Matter* **1997**, *9*, 8795.
(5) Kownacki, J. P.; Diep, H. T. *Phys. Rev. E* **2002**, *66*, 066105.
(6) Goel, V.; Chatterjee, T.; Bombalski, L.; Yurekli, K.; Matyjaszewski, K.; Krishnamoorti, R. *J. Polym. Sci., Part B: Polym. Phys.* **2006**, *44*, 2014.
(7) Ren, J.; Krishnamoorti, R. *Macromolecules* **2003**, *36*, 4443.
(8) Hsied, A. J.; P. Moy, F. L. B.; Madison, P.; Napadensky, E.; Ren, J.; Krishnamoorti, R. *Polym. Eng. Sci.* **2004**, *44*, 825.
(9) Xu, L.; Reeder, S.; Thopasridharan, M.; Ren, J.; Shipp, D. A.; Krishnamoorti, R. *Nanotechnology* **2005**, *16*, S514.
(10) Katsnelson, M. I.; Novoselov, K. S.; Booth, T. J.; Roth, S.; Meyer, J. C.; Geim, A. K. *Nature* **2007**, *446*, 60.
(11) Hwa, T.; Kokufuta, E.; Tanaka, T. *Phys. Rev. A* **1991**, *44*, R2235.
(12) Wen, X.; Garland, C. W.; Hwa, T.; Kardar, M.; Kokufuta, E.; Li, Y.; Orkisz, M.; Tanaka, T. *Nature* **1992**, *355*, 426.
(13) Spector, M. S.; Naranjo, E.; Chiruvolu, S.; Zasadzinski, J. A. *Phys. Rev. Lett.* **1994**, *73*, 2867.
(14) Iijima, S. *Nature* **1991**, *354*, 56.
(15) Iijima, S.; Brabec, C.; Maiti, A.; Bernholc, J. *J. Chem. Phys.* **1996**, *104*, 2089.
(16) Baughman, R. H.; Zakhidov, A. A.; de Heer, W. A. *Science* **2002**, *297*, 787.
(17) Stupp, S. I.; Son, S.; Lin, H. C.; Li, L. S. *Science* **1993**, *259*, 59.
(18) Kantor, Y.; Kardar, M.; Nelson, D. R. *Phys. Rev. Lett.* **1986**, *57*, 791.
(19) Kantor, Y.; Kardar, M.; Nelson, D. R. *Phys. Rev. A* **1987**, *35*, 3056.
(20) Kardar, M.; Nelson, D. R. *Phys. Rev. Lett.* **1987**, *58*, 1289.
(21) Abraham, F. F.; Rudge, W. E.; Plischke, M. *Phys. Rev. Lett.* **1989**, *62*, 1757.
(22) Grest, G. S.; Murat, M. *J. Phys.* (*Paris*) **1990**, *51*, 1415.
(23) Grest, G. S. *J. Phys. I* **1991**, *1*, 1695.
(24) Kantor, Y.; Kremer, K. *Phys. Rev. E* **1993**, *48*, 2490.
(25) Liu, D.; Plischke, M. *Phys. Rev. A* **1992**, *45*, 7139.
(26) Grest, G. S.; Petsche, I. B. *Phys. Rev. E* **1994**, *50*, R1737.
(27) Punkkinen, O.; Flach, E.; Vattulainen, I.; Ala-Nissila, T. *J. Chem. Phys.* **2006**, *122*, 094904.
(28) Shannon, S. R.; Choy, T. C. *Phys. Rev. Lett.* **1997**, *79*, 1455.
(29) Vianney, J. M.; Koelman, A. *Phys. Rev. Lett.* **1990**, *64*, 1915.
(30) Chaieb, S.; Natrajan, V. K.; El-rahman, A. A. *Phys. Rev. Lett.* **2006**, *96*, 078101.
(31) Douglas, J. F. *Phys. Rev. E* **1996**, *54*, 2677.
(32) Pandey, R. B.; Anderson, K. L.; Farmer, B. L. *J. Polym. Sci., Polym. Phys.* **2005**, *43*, 3478.
(33) Pandey, R. B.; Anderson, K. L.; Heinz, H.; Farmer, B. L. *J. Polym. Sci., Polym. Phys.* **2005**, *43*, 1041.
(34) Pandey, R. B.; Anderson, K. L.; Farmer, B. L. *J. Polym. Sci., Polym. Phys.* **2006**, *44*, 2512.
(35) Pandey, R. B.; Anderson, K. L.; Farmer, B. L. *Phys. Rev. E* **2007**, *75*, 061913.
(36) Blumstein, A.; Blumstein, R.; Vanderspurt, T. H. *Colloid Interface Sci.* **1969**, *31*, 236.
(37) Blumstein, A.; Herz, J.; Sinn, V.; Sardon, C. *C. R. Acad. Sci.* **1958**, *246*, 1856.
(38) Van Workum, K.; Douglas, J. F. *Phys. Rev. E* **2006**, *73*, 031502.
(39) Yamakawa, H. *Modern Theory of Polymer Solutions*; Harper & Row: New York, 1971.
(40) Sinsawat, A.; Anderson, K. L.; Vaia, R. A.; Farmer, B. L. *J. Polym. Sci., Part B: Polym. Phys.* **2003**, *41*, 3272.
(41) Knauert, S. T.; Douglas, J. F.; Starr, F. W. *J. Polym. Sci., Part B: Polym. Phys.* **2007**, *9*, 1882.
(42) Grest, G. S.; Kremer, K. *Phys. Rev. A* **1986**, *33*, 3628.
(43) Tolla, D. D.; Ronchetti, M. *Phys. Rev. E* **1993**, *48*, 1726.

(44) Tuckerman, M.; Berne, B. J.; Martyna, G. J. *J. Chem. Phys.* **1992**, *97*, 1990.
(45) Doi, M.; Edwards, S. F. *The Theory of Polymer Dynamics*; Clarendon Press: Oxford, U.K., 1986.
(46) de Gennes, P.-G. *Scaling Concepts in Polymer Physics*; Cornell: Ithaca, NY, 1979.
(47) The uncertainty here provides a qualitative estimate of the range of exponent values consistent with the data.
(48) Radzihovsky, L.; Toner, J. *Phys. Rev. Lett.* **1995**, *75*, 4752.
(49) Radzihovsky, L.; Toner, J. *Phys. Rev. E* **1998**, *57*, 1063.
(50) Bowick, M.; Falcioni, M.; Thorleifsson, G. *Phys. Rev. Lett.* **1997**, *79*, 885.
(51) Abraham, F. F.; Kardar, M. *Science* **1991**, *252*, 419.
(52) Mansfield, M. L.; Douglas, J. F.; Garboczi, E. J. *Phys. Rev. E* **2001**, *6*, 61401.
(53) Douglas, J. F.; Garboczi, E. J. *Adv. Chem. Phys.* **1995**, *91*, 85.
(54) Hubbard, J. B.; Douglas, J. F. *Phys. Rev. E* **1993**, *47*, R2983.
(55) Jackson, J. D. *Classical Electrodynamics*; Wiley: New York, 1975.
(56) Douglas, J. F.; Zhou, H.-X.; Hubbard, J. B. *Phys. Rev. E* **1994**, *49*, 5319.
(57) Einstein, A. *Ann. Phys.* **1906**, *19*, 289.
(58) Ford, T. F. *J. Phys. Chem.* **1960**, *64*, 1168.
(59) Mansfield, M. L.; Douglas, J. F. *Phys. Rev. E*, in press.
(60) Mansfield, M. L.; Douglas, J. F. *Condens. Matter Phys.* **2002**, *5*, 249.
(61) Popova, H.; Milchev, A. *J. Chem. Phys.* **2007**, *127*, 194903.